Enabling Real-time Indoor Tracking of IoT Devices Through Visible Light Retroreflection

Sihua Shao, *Member, IEEE,* Abdallah Khreishah, *Senior Member, IEEE,* and Issa Khalil, *Senior Member, IEEE*

Abstract—Visible light communication (VLC)-based indoor localization approaches enjoy many advantages, such as utilizing ubiquitous lighting infrastructure, high location accuracy, and no interruption to RF-based devices. However, existing VLC-based localization methods lack a real-time backward channel from the device to landmarks and necessitate computation at the device, which make them unsuitable for real-time tracking of small IoT devices. In this paper, we propose and prototype RETRO, that establishes an almost zero-delay backward channel by retroreflection. RETRO localizes passive IoT devices without requiring computation and heavy sensing (e.g., camera) at the devices. Multiple photodiodes (i.e., landmarks) are mounted on *any single unmodified* light source to sense the retroreflected optical signal (i.e., location signature). We derive a closed-form expression, which is validated by experiments and ray tracing simulations, for the reflected optical power relative to the location and the orientation of the retroreflector. The expression is applied to a received signal strength indicator and trilateration based localization algorithm. Extensive experiments demonstrate centimeter-level location accuracy and single-digit angular error. For practicality concern, to mitigate the thickness problem of a single retroreflector, the capabilities of different retroreflector arrays are studied. The range of the localization system is theoretically evaluated for different light emission patterns.

Index Terms—Indoor localization, retroreflector, visible light localization, IoT localization.

1 Introduction

Indoor localization is an important field of application for Internet-of-Things (IoT), for example in warehouses, airports, railway stations, shopping centers, trade fairs, hospitals, offices and factories. Existing indoor localization approaches can be divided into two categories: client-based and server-based indoor localization. Client-based indoor localization, which is mainly suitable for navigation, is done directly on the device. Through receiving beacons from one or multiple access points (APs), the device self-determines its position in local coordinates system. Server-based indoor localization, which is suitable for asset and personal tracking, requires the device to send unique identity information to specific hardware, which can capture the information and forward them to a server to calculate the device's position.

Real-time locating system (RTLS) [1] is a typical field of application for server-based indoor localization. RTLS is used to automatically identify and track the location of objects or people in real time. Applications of RTLS include but are not limited to locating assets in a facility, such as tracking of medical instruments at a clinic, vehicles in industrial facilities and goods in retail shops; locating people, such as providing details about visitor flows, employer checking the current position of employees, and locating customers in a restaurant for food delivery; remote control, such as utilizing unmanned aerial vehicles (UAVs) for tunnel deflection inspection, stadium sports filming and disabled guidance. The remote-controlled UAV relies on joint localization and communication system to track the location and send control command at the same time.

Visible light communication (VLC) or LiFi can be used as a localization technology [2], [3], [4], [5], [6], [7]. LED or fluorescent lamps send out imperceptible flickering light that can be captured by a smart phone camera or photodetector. The information of received optical signal strength, angle-of-arrival, polarization and light distribution patterns can be leveraged for localizing light sensing enabled devices. Relying on extensively and homogeneously deployed lighting infrastructure, VLC-based localization approaches only require low-cost additional light source driver [2], [3], [7], or even do not need additional hardware [5], [6]. Thanks to the dominant line-of-sight (LOS) signal and incidence angle sensitive propagation path loss property, VLC-based localization can easily achieve sub-meter accuracy and also detect the orientation of devices [3]. Although VLC-based localization embraces many advantages, the absence of a real-time backward channel from devices to APs restricts the VLC methods to client-based indoor localization, which leads to impractical requirement of computation or heavy sensing (e.g., camera) on small IoT devices. Autonomously sending location and orientation information to the server results in inevitable latency to real-time tracking as well as unnecessary burden on IoT devices. It is worth noticing that computer-vision-based tracking methods [8] can localize various objects without even placing any device on the objects. However, the computer-vision-based tracking methods require cameras to be installed on the ceiling, which may lead to problems related to privacy. The proposed localization system is expected to be deployed at places such

- *S. Shao and A. Khreishah are with the Department of Electrical and Computer Engineering, New Jersey Institute of Technology, Newark, New Jersey, USA.*
  E-mail: ss2536@njit.edu, abdallah@njit.edu
- *I. Khalil is with Qatar Computing Research Institute, Doha, Qatar.*
  E-mail: ikhalil@qf.org.qa
- *Part of this work was presented in IEEE INFOCOM 2018.*

Manuscript received XX-XX-XXXX ; revised XX-XX-XXXX.

This article has been accepted for publication in a future issue of this journal, but has not been fully edited. Content may change prior to final publication. Citation information: DOI 10.1109/TMC.2019.2901665, IEEE Transactions on Mobile Computing

as office, hospital and home where the users do not prefer to be exposed to cameras. Also the methods need additional known-location anchors to be deployed in order to localize a device in a global reference frame.

To address the above problems of VLC-based approaches and also the problems of RF-based approaches (i.e., power constraint limits the distance a wireless signal can travel and requires huge infrastructure support in terms of access points and fronthaul links to achieve small frequency reuse distances), which make conventional VLC/RF-based solutions unsuitable for the applications of RTLS such as asset tracking, we propose and prototype a retroreflector-based visible light localization system that we name RETRO. The retroreflector is a light-weight small device, which is capable of reflecting light back to its source with minimal scattering. Therefore, by mounting small-size light sensors, such as photodiodes (PDs), on infrastructural lamps, we can establish a backward channel from the retroreflector to VLC APs (i.e., lamps). In order to send unique identity information to APs, we add a liquid crystal display (LCD) shutter, which consumes only tens of μW with its driver circuit [9], [10], [11], on the retroreflector to modulate and distinguish the reflected light from different IoT devices. The light-weight retroreflector along with an LCD shutter and its control unit can be installed on a passive IoT device to execute VLC-based real-time localization. The retroreflector can be realized by corner-cube, retroreflective sheeting [12] or even retroreflective spray paint [13]. In this work, we mainly study the corner-cube retroreflector and its extension (i.e., retroreflector array). RETRO enjoys not only all the advantages (e.g., especially high location accuracy) provided by conventional VLC-based localization approaches, but also four unique and superior features: 1) RETRO can be implemented on *any single slightly modified* light source; 2) immediate feedback from the retroreflector minimizes the latency of a centralized control of IoT devices; 3) RETRO is capable of localizing passive IoT devices with ultra-low power and no computational capability at the devices; 4) RETRO establishes a visible light uplink channel, which makes joint localization and communication possible without an additional uplink RF channel.

In this paper, we utilize the received signal strength indicator (RSSI) and trilateration based localization algorithm (Sec. 4) to localize the retroreflector. An overview of our proposed localization system is presented in Sec. 2. The RSSI resulted from the retroreflected light is theoretically analyzed (Sec. 3) and experimentally validated (Sec. 5). Based on experimental evaluation (Sec. 6), our proposed RETRO system can achieve centimeter-level localization accuracy and single-digit angular error. For the cases where it is very difficult to measure the experimental data due to the hardware limitation of the commercial off-the-shelf (COTS) corner-cube retroreflector, the theory (Sec. 3) is further validated by a ray tracing simulator (Sec. 7.1). For practicality concern, to mitigate the thickness problem of a single corner-cube retroreflector, the capabilities of different retroreflector arrays are studied in Sec. 7.2. The impact of different light emission patterns on the range of the localization system is evaluated in Sec. 7.3. The limitations of our current system and potential future directions are discussed in Sec. 8. We review the related RF-based and VLC-based localization works in Sec. 9 and conclude our work in Sec. 10.

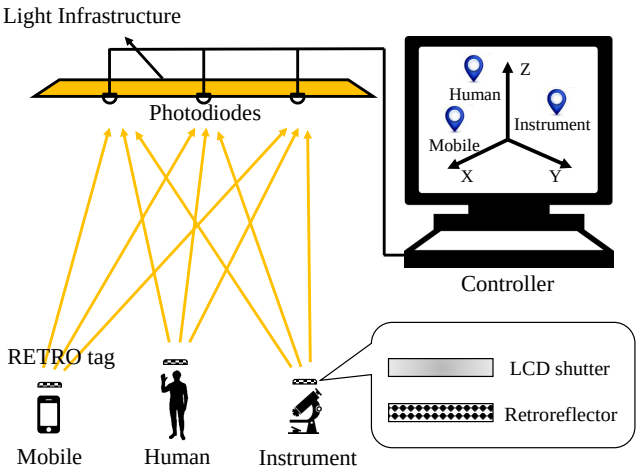

Fig. 1: System overview

In summary, we make four key contributions:

- To the best of our knowledge, RETRO is the first system that enables 3D real-time tracking using the VLC-based localization approach. Relying on *any single slightly modified* light source, RETRO is capable of localizing passive IoT devices without requiring computation or heavy sensing on the IoT device with minimum latency.
- We theoretically derive a closed-form expression for estimating retroreflected optical power from retroreflectors under Lambertian light source and experimentally validate the theory. Experimental results match theoretical results very well w.r.t different locations and orientations of the retroreflector. For the cases where it is very difficult to measure the experimental data, a ray tracing simulator is utilized to further validate the theory.
- Based on the characterization of received optical power from the retroreflector and an RSSI and trilateration based localization algorithm, we perform extensive experiments to evaluate the location and orientation accuracy of our proposed RETRO system and observe centimeter-level location accuracy (i.e., location error within 4.5 cm with the height of 1.5 meters) and up to 1° orientation error.
- Taking practical deployment into consideration, we further investigate the thickness of the retroreflector and the range of the localization system. To mitigate the thickness problem of a single retroreflector caused by the structure of corner-cube, different retroreflector arrays are studied with respect to the retroreflected optical power. The range of the localization system is evaluated in terms of different light emission patterns.

2 Overview of the Localization Approach

In this work, RSSI and trilateration based localization approach [2] is used to estimate the position and orientation of an IoT device equipped with a retroreflector in the

This article has been accepted for publication in a future issue of this journal, but has not been fully edited. Content may change prior to final publication. Citation information: DOI 10.1109/TMC.2019.2901665, IEEE Transactions on Mobile Computing

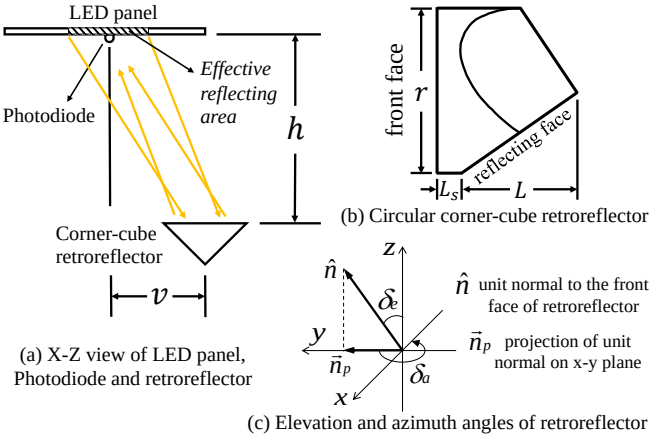

(a) X-Z view of LED panel, Photodiode and retroreflector

(b) Circular corner-cube retroreflector

(c) Elevation and azimuth angles of retroreflector

Fig. 2: Illustration of system parameters

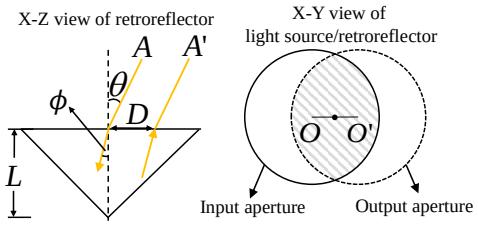

Fig. 3: Displacement of input and output apertures caused by the oblique angle of incidence to the retroreflector

global frame of reference. As shown in Fig. 1, multiple PDs (i.e., landmarks) are mounted on one light source or multiple light sources to sense the reflected optical signal strength from a retroreflector (RETRO tag). Regarding the capability of sensing the retroreflected optical signals, there is no restriction on the precision of the location of the PDs as long as light is evenly distributed on the light emitting surface where the PDs are attached to. An LCD shutter (Sec. 6.1) covering the front face of retroreflector produces unique signal frequency for each retroreflector to distinguish the reflected light from multiple IoT devices and from environmental reflections. The received signal strength of each PD, which is facing downward and sensing the retroreflected optical signals within a certain region under the light source, is utilized by the controller to compute the location and orientation of each RETRO tag which indicates the location and orientation of the corresponding IoT device. As the retroreflector changes its location and orientation, the received signal strength of each PD varies correspondingly. One reason to utilize retroreflector in our proposed system is that light from different light sources can be reflected back and hence isolated. Without this feature, the system would have problems tackling the weighted sum of the reflected optical signals from multiple light sources. In order to investigate the relationship between the location and orientation of the retroreflector and the received signal strength of each PD, we need to not only use the free space optical propagation model, but also characterize the area of light source, from which the light rays are retroreflected back to the corresponding PD. We call this area the *effective reflecting area*. In the next section, we theoretically study the effective reflecting area w.r.t different locations and orientations of the retroreflector.

3 Analysis for Received Optical Power

3.1 System parameters

To derive a closed-form expression of retroreflected optical power, we define the following system parameters: 1. semi-angle at half power of light source, $\psi_{1/2}$. An evenly distributed light source can be viewed as infinite small lighting spots, where all the spots have the same value of $\psi_{1/2}$. 2. refractive index of coating material of retroreflector, n. 3. length of retroreflector, L. 4. recessed length of retroreflector, L_s. 5. diameter of retroreflector's front face, r. 6. effective sensing area of PD, A_s. 7. transmitted optical power multiplied by reflector loss (reflector loss includes the transmission loss of the coating material and the reflection loss of each reflection surface), P_t. 8. Lambertian index, ml. 9. vertical distance between light source plane and the front face of retroreflector, h. 10. horizontal distance between the PD and the retroreflector, v. 11. elevation angle of the front face of the retroreflector, δ_e. 12. azimuth angle of the front face of the retroreflector, δ_a. The parameters are illustrated in Fig. 2.

To make the derivation clearer, we divide it into two steps: in the first step we consider a special case where the elevation and azimuth angles are both zero, and we analyze the boundary of the effective reflecting area based on the symmetry property of the incident and retroreflected rays; in the second step we study the other case where the elevation and azimuth angles are arbitrary, and since the derivation in case 1 cannot be simply applied to case 2, we create a virtual light source plane and utilize oblique projection to analyze the boundary of effective reflecting area. Note that the light source we consider here is a flat LED panel with evenly distributed light across the face of the panel. The derivation can be extended to the case where unevenly distributed light sources are considered.

3.2 Zero elevation and azimuth angles case

The distance between the PD and the retroreflector is

$$d = \sqrt{h^2 + v^2}. \tag{1}$$

Consider the scenarios when the distance between the light source and the retroreflector is much larger than the size of retroreflector, the radiance angles of all rays that are reflected back to the PD can be approximated to be the same. Also, since the rays are reflected back along a vector that is parallel to but opposite in direction from the rays' source, the incidence angle to the PD is the same as the radiance angle. The value of radiance and incidence angles is

$$\theta = \tan^{-1} \frac{v}{h}. \tag{2}$$

According to Snell's law, the refracted angle is

$$\phi = \sin^{-1} \frac{\sin \theta}{n}. \tag{3}$$

As shown in Fig. 3, ray A incident on the center of the front face is retroreflected as ray A'. The points of intersection of A and A' with the front face are separated by D. Note that if $\theta = 0$, then $D = 0$. The solid line (circle

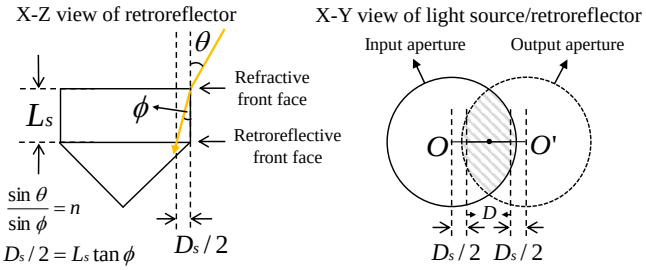

Fig. 4: Displacement of input and output apertures caused by the recession

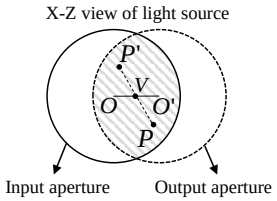

Fig. 5: Symmetry of incident ray and retroreflected ray

O), which is the shape of the retroreflector face, is called the input aperture, and the dotted line (circle O'), which is giving the outline of the retroreflected beam, is the output aperture. We have $\overline{OO'} = D$. The intersection of the input and output apertures is the active reflecting area [14]. Note that in [14], the active reflecting area is given on the plane of the front face of the retroreflector to analyze the proportion of incident beam (i.e., a set of parallel light rays emitted from a point light source) that can be retroreflected. If the three reflecting surfaces of the corner-cube retroreflector are not perfectly perpendicular, the retroreflected light beam will be misaligned with incident beam and scattered to some extent. The typical applications based on the well studied properties of corner-cube retroreflector include laser-based ranging system, road sign and vehicle recognition. The factor that all the applications care about is the quantization of the light intensity attenuation caused by the retroreflection if the receiver is placed at a specific direction to sense the retroreflected light. The theoretical analysis in [14] cannot be directly applied to Lambertian light source, from which the emitted light rays are not parallel. We have uncountable point light sources and the relative positions of the receiver (i.e., PD) to the uncountable point light sources are all different. Therefore, in this paper, we utilize the concept of active reflecting area, as illustrated in Fig. 3, on the *plane of light source* to tackle two most challenging problems: i) for all the incident beams, which of them can be retroreflected back to the PD; 2) how to take the integral of all the beams that can be retroreflected back to the PD. Assume a set of parallel rays incident on the front face of retroreflector with angle θ are emitted from the area within circle O on the light source plane, then only the rays from the intersection of circle O and O' are retroreflected. According to [14] (Page 10), the displacement of input and output apertures caused by the incidence angle θ is

$$D = 2L \tan \phi. \tag{4}$$

As shown in Fig. 4, the recession wall shadows the front face of the retroreflector at an oblique incidence angle. The recession leads to additional displacement of input and output apertures D_s ([14] Page 14). From the top view of the light source, the distance between circle O and circle O' is further increased by D_s. Therefore, the active reflecting area on the plane of the light source is further reduced due to recession. The displacement of input and output apertures caused by recession is

$$D_s = 2L_s \tan \phi. \tag{5}$$

Given the displacements D and D_s, now we study which light rays are reflected to the PD. As shown in Fig. 5, V is the midpoint of $\overline{OO'}$, where $\overline{OO'} = D + D_s$. Recall that the shaded area contains a set of parallel rays, of which the incidence angles to the front face of the retroreflector are all θ, and this set of parallel rays can be retroreflected back to the shaded area. Suppose a ray from point P' is one of the parallel rays, the retroreflected ray intersects with the shaded area at point P, which is an equal distance on the other side of vertex V ([14] Page 9). Therefore, if P is where the PD is located at, and considering the parallel rays (radiance angles are all θ) from circle O, the ray from point P' is the one that can be retroreflected to the PD.

On the light source plane, there are uncountably many small circles with the same size as that of circle O. Each small circle contains a set of parallel rays, whose radiance angle depends on the location of the corresponding small circle. If the PD is located in the shaded area of a small circle, in the corresponding set of parallel radiant rays, there exists a ray that can be reflected back to the PD. Therefore, there are uncountably many small circles, in each of them there exists a ray that can be reflected back to the PD. The intersection of the set of rays that can be reflected back to the PD with the *plane of light source* is the *effective reflecting area*. In other words, the effective reflecting area is an area of the light emitting surface around the PD, from which the emitted optical rays are retroreflected back to the PD. Note that if the size of the PD is comparable to the size of the front face of the retroreflector, the PD itself will block a large portion of the effective reflecting area and thereby approximating the PD as a point in the theoretical derivation will cause non-negligible approximation error. This issue will be further discussed in Sec. 5 and Sec. 8.

Theorem 1. If the incidence angles of the light rays that can be retroreflected to the PD are approximated to be the same as the radiance angle θ, given two displacements D and D_s, and the diameter of retroreflector r, the size of effective reflecting area is the intersection of two circles, of which the radii are r and the distance between them is $2(D + D_s)$.

Proof: In order to evaluate the size of the effective reflecting area, we need to figure out its boundary. Consider a special case in Fig. 5, where P is on circle O, P' will be located on circle O' due to symmetry. It can be proved that for each point P'_m on $\overline{PP'}$ there exists a circle O and a circle O', where the intersection of two circles includes both P'_m and P, and the symmetry in Fig. 5 holds. Therefore, for every point on $\overline{PP'}$ there exists a ray that can be retroreflected to P. P' is the furthest point (from which there exists a ray that can be retroreflected to P) away from P along the

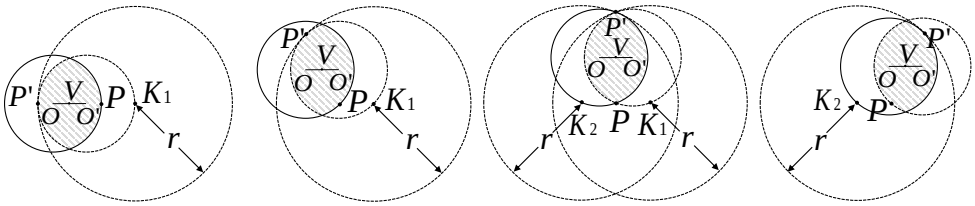

(a) P' is on circle K_1 (b) P' is on circle K_1 (c) P' is on circle K_1 and K_2 (d) P' is on circle K_2

Fig. 6: Four cases when using symmetry of incident ray and retroreflected ray to analyze the boundary of effective reflecting area

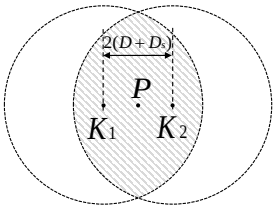

Fig. 7: Effective reflecting area

direction of $\overrightarrow{PP'}$. Since the incidence angles of the light rays that can be retroreflected to the PD are approximated to be the same, the separation distances and directions of circle O' for all the possible locations of circle O are the same. Therefore, if we rotate the intersection of circle O and circle O' (i.e., the shaded area in Fig. 5) around P and keep P on the boundary of the intersection, considering P as the location of PD, the trajectory of P' will be the boundary of the effective reflecting area.

In Fig. 6, we use two big circles (K_1 and K_2), of which the radii are r (i.e., diameter of circle O), to analyze the trajectory of P'. The distances $\overline{PK_1}$ and $\overline{PK_2}$ are both equal to $\overline{OO'}$, and both $\overline{PK_1}$ and $\overline{PK_2}$ are parallel to $\overline{OO'}$. In Fig. 6 (a), $\angle P'K_1P = 0°$, since $\overline{PP'} = r - \overline{OO'}$ and $\overline{PK_1} = \overline{OO'}$, $\overline{P'K_1} = r$ which indicates that P' is on circle K_1. In Figs. 6 (b), (c) and (d), it can be proved by the similarity between $\triangle P'VO'$ and $\triangle P'PK_1$ (or $\triangle P'VO$ and $\triangle P'PK_2$) that $\overline{P'K_1} = r$ (or $\overline{P'K_2} = r$), which indicates that P' is either on circle K_1 or on circle K_2 when we rotate the intersection of circle O and O' (i.e., the shaded area in Fig. 6) around P and keep P on the intersection boundary. Therefore, the trajectory of P' is the boundary of the intersection of circle K_1 and K_2. The effective reflecting area is the shaded area in Fig. 7. □

Given D and D_s, the ratio of effective reflecting area to the maximum effective reflecting area (i.e., when $D + D_s = 0$) is

$$\alpha = \frac{2r^2(\cos^{-1}\frac{D+D_s}{r} - \frac{D+D_s}{r}\sin(\cos^{-1}\frac{D+D_s}{r}))}{\pi r^2}. \quad (6)$$

Since the radiance angle of the effective reflecting area is equal to the incidence angle to the PD and the propagation distance is $2d$, according to the free space optical path loss model in [15], the received optical power is

$$P_r = P_t \frac{(ml+1)A_s}{8\pi d^2}\cos^{ml+1}\theta g(\theta)\alpha, \quad (7)$$

where $g(\theta)$ is the concentrator gain.

3.3 Arbitrary value of elevation and azimuth angles case

If the front face of the retroreflector is not parallel to the light source plane, we cannot directly apply the analysis in case 1 (i.e., when $\delta_e = 0$ and $\delta_a = 0$) by simply varying the incidence angle to the front face of retroreflector. This is because the shape of the front face of retroreflector is different from its oblique projection along the direction of retroreflected light rays on the light source plane.

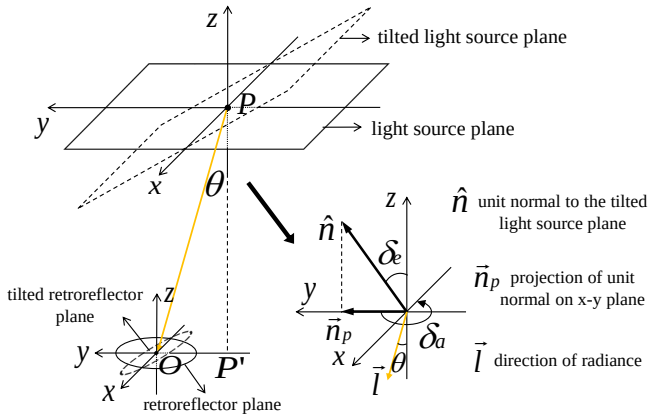

Fig. 8: A virtual light source plane to illustrate Theorem 2

As shown in Fig. 8, the retroreflector plane is parallel to the light source plane. Point P is where the PD is located at. Point P' is the projection of P on the retroreflector plane. Point O is the center of the front face of retroreflector. We use $\overrightarrow{P'O}$ as the direction of y axis and form the 3D coordinate systems for both the retroreflector and the light source. If the retroreflector changes its orientation and its front face is on a tilted retroreflector plane, we create a virtual tilted light source plane, which is parallel to the tilted retroreflector plane. The intersection line of the real light source plane and the virtual tilted light source plane crosses point P. Now we can perform the same analysis in case 1 (i.e., when $\delta_e = 0$ and $\delta_a = 0$) on the tilted light source plane based on the new incidence angle to the front face of tilted retroreflector, which is formed by the normal $\hat{n}$ to the tilted retroreflector plane and $\overrightarrow{OP}$). Therefore, the size of a virtual effective reflecting area S on the tilted light source plane can be derived from (6).

The virtual effective reflecting area S on the tilted light source plane contains a set of rays that can be retroreflected back to the PD. These rays are approximated to be parallel to $\overrightarrow{PO}$. In order to figure out the effective reflecting area S' on the real light source plane, we need to derive the oblique projection of S on the real light source plane along the direction of $\overrightarrow{PO}$. As shown in Fig. 8, in the coordinate system of light source, $\hat{n}$ is the unit normal to the tilted light source plane, and $\overrightarrow{n_p}$ is the projection of $\hat{n}$ on x-y plane. Elevation angle δ_e is formed by $\hat{n}$ and the z axis, azimuth angle δ_a is formed by $\overrightarrow{n_p}$ and the y axis, $\overrightarrow{l}$ denotes the direction of $\overrightarrow{PO}$, and radiance angle θ is formed by $\overrightarrow{l}$ and the z axis.

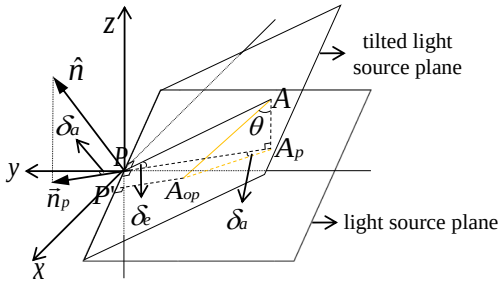

Fig. 9: Point A is on the tilted light source plane and its oblique projection A_{op} is on the light source plane

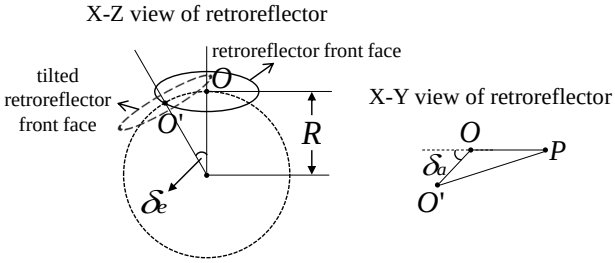

Fig. 10: When rotation center is not coincident with the center of the front face of retroreflector

***Theorem* 2.** Given θ, δ_e and δ_a, the ratio of S' and S, β, is equal to $\cos\delta_e - \sin\delta_e \tan\theta \cos\delta_a$.

Proof: In Fig 9, point A is on the tilted light source plane, point A_p is the projection of point A on the real light source plane, and point A_{op} is the oblique projection of point A on the real light source plane along the direction of $\overrightarrow{l}$, where $\overline{AP}$, $\overline{A_pP}$ and $\overline{A_{op}P'}$ are all perpendicular to the intersection line of the real light source plane and the virtual tilted light source plane. The direction of $\overrightarrow{A_pP}$ is the same as that of $\overrightarrow{n_p}$. Therefore, $\angle APA_p = \delta_e$, $\angle A_{op}AA_p = \theta$, $\angle PA_pA_{op} = \delta_a$. It can be proved by the principle of calculus that $\frac{S'}{S} = \frac{\overline{A_{op}P'}}{\overline{AP}}$. Since $\overline{A_pP} = \overline{AP}\cos\delta_e$, $\overline{A_pA_{op}} = \overline{AA_p}\tan\theta = \overline{AP}\sin\delta_e\tan\theta$ and $\overline{A_{op}P'} = \overline{A_pP} - \overline{A_pA_{op}}\cos\delta_a = \overline{AP}\cos\delta_e - \overline{AP}\sin\delta_e\tan\theta\cos\delta_a$, we have

$$\beta = \frac{S'}{S} = \frac{\overline{A_{op}P'}}{\overline{AP}} = \frac{\overline{AP}\cos\delta_e - \overline{AP}\sin\delta_e\tan\theta\cos\delta_a}{\overline{AP}} = \cos\delta_e - \sin\delta_e\tan\theta\cos\delta_a \quad (8)$$

□

Substituting the incidence angle to the front face of the tilted retroreflector (i.e., formed by the normal $\hat{n}$ to the tilted retroreflector plane and $\overrightarrow{OP}$ in Fig. 8) to (4) and (5), we can find D and D_s for the tilted retroreflector. Substituting D and D_s for the tilted retroreflector to (6), we can find the ratio of the effective reflecting area and the maximum effective reflecting area α on the virtual tilted light source plane. Therefore, the received optical power

$$P_r = P_t \frac{(ml+1)A_s}{8\pi d^2}\cos^{ml+1}\theta g(\theta)\alpha\beta. \quad (9)$$

3.4 Practical concern

In practice, the retroreflector may not rotate around the center of its front face. As shown in Fig. 10, the distance between the front face of the retroreflector and the rotation center is R. Therefore, the new vertical distance between the light source and the retroreflector is $h_{new} = h + R(1-\cos\delta_e)$. The new horizontal distance between the PD and the retroreflector is

$$v_{new} = \overline{O'P} = \sqrt{(\overline{OP} + \overline{OO'}\cos\delta_a)^2 + (\overline{OO'}\sin\delta_a)^2} = \sqrt{(v + R\sin\delta_e\cos\delta_a)^2 + (R\sin\delta_e\sin\delta_a)^2}$$

In order to recompute P_r in (9), we substitute h_{new} and v_{new} into (1)-(6) and (8), and get the new values of d, θ, α and β.

4 Localization Algorithm

Given n PDs mounted on the light source plane, we can apply (9) to form constraints on measured received optical power and distances between the PDs and the retroreflector, as well as the azimuth and elevation angles of the retroreflector,

$$P_{ri} = P_t \frac{(ml+1)A_{si}}{8\pi {d_i}^2}\cos^{ml+1}\theta_i g(\theta_i)\alpha_i\beta_i, i = 1, 2, ..., n. \quad (10)$$

Let the 3D coordinates of the retroreflector and the i-th PD be (x_0, y_0, z_0) and (x_i, y_i, z_i), respectively. We have the horizontal distance between the i-th PD and the retroreflector $v_i = \sqrt{(x_0-x_i)^2 + (y_0-y_i)^2}$ and the vertical distance between the light source plane and the front face of the retroreflector $h = |z_0 - z_i|$. Recall that the azimuth and elevation angles of the retroreflector are denoted by δ_a and δ_e, respectively. Therefore, there are five unknowns x_0, y_0, z_0, δ_a and δ_e when we estimate the position and orientation of the retroreflector. With five or more PDs with known 3D coordinates, we can uniquely determine all the five unknowns. Note that since the landmarks in RETRO system are PDs instead of light sources (i.e., landmarks in conventional VLC-based localization approaches), RETRO is able to localize devices with *any single slightly modified* light source. The localization is framed as an optimization process trying to minimize the sum of square errors between the left and right hand sides of (10),

$$\overrightarrow{s}_{opt} = \arg\min_{s} \sum_i f_i(\overrightarrow{s})^2,$$

where $\overrightarrow{s} = (x_0, y_0, z_0, \delta_a, \delta_e)$ and

$$f_i(\overrightarrow{s}) = P_{ri} - P_t \frac{(ml+1)A_{si}}{8\pi {d_i}^2}\cos^{ml+1}\theta_i g(\theta_i)\alpha_i\beta_i, i = 1, 2, ..., n.$$

To accelerate the search process for the above non-linear least square optimization problem, the widely-used Levenberg-Marquardt algorithm [4] is adopted. Levenberg-Marquardt algorithm reduces the search space by searching along the direction of the gradient, which moves toward the local minimum. The initial values of unknowns are generated randomly and we run the localization algorithm several times to avoid local minima. The efficiency of the Levenberg-Marquardt algorithm is proved in [4], which can converge to a local minimum in several milliseconds. In our experiments, we show that the localization algorithm can generate very high location and orientation accuracy.

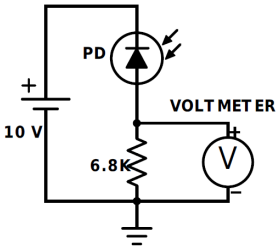

Fig. 11: Light intensity measurement circuit

5 Experiment Based Validation of the Derivation of Received Optical Power

5.1 Testbed settings

We utilize a flat LED panel with evenly distributed light as the light source, which is a COTS LED Troffer 2x2 FT (35W, 4000K, 3770 Lumens) provided by Hyperikon. To estimate $\psi_{1/2}$ of the LED panel, we manually restrict the effective illumination area to a small spot and find out that $\psi_{1/2} = 60°$, and the Lambertian index $ml = -\frac{\ln 2}{\ln(\cos \psi_{1/2})}$. The circular retroreflector PS976 (uncoated) is manufactured by Thorlabs [16]. The substrate material is BK7 grade A, according to [17], with a refractive index $n = 1.51$ for visible light wavelength. According to [16], the length of retroreflector $L = 35.7\ mm$, the length of recession $L_s = 6.3\ mm$ and the diameter of the front face of retroreflector $r = 50\ mm$. The PD S6968 is provided by Hamamatsu Photonics [18], and $A_s = 150\ mm^2$. Note that the size of PD is much less than the size of front face of the retroreflector (i.e., around 2000 mm^2). The initial calibration is needed to determine the value of P_t, which can be estimated by fitting the measured received optical signal strength at different heights to the theoretical results (typically three measurements are sufficient). The one-time measurements take into account the constant signal attenuation caused by the coating material, the reflecting surfaces and the LCD shutter (when the shutter is applied in Sec. 6).

The PD works in photoconductive mode to measure the light intensity. As shown in Fig. 11, the PD is driven by a 10 V DC and cascaded with a 6.8kΩ resistor. When the PD is reverse biased, for a given spectral distribution, the generated photocurrent is linearly proportional to the illuminance. Therefore, the output voltage of the resistor cascaded with the PD is linearly proportional to the received optical power P_r. The output voltage is measured by a multimeter. To get rid of the environmental reflection, we perform two measurements with each location or orientation. In the first measurement, we use an opaque chip to cover the front face of the retroreflector and measure the output voltage which is only contributed by the environmental reflection. In the second measurement, we remove the opaque chip to measure the output voltage which is contributed by both the environmental reflection and the reflection of the retroreflector. Referring to Fig. 1-10 in [19], the illuminance level resulting in saturation is highly related to the reverse voltage and the output voltage is linearly proportional to the illuminance before reaching to the upper limit of the linearity (i.e., saturation). Fig. 1-10 in [19] indicates that if the output voltage still increases as the illuminance increases,

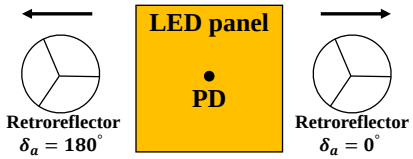

Fig. 12: Explanation of light leaking problem (only when $\delta_a = 0°$, total internal reflection property holds when v increases)

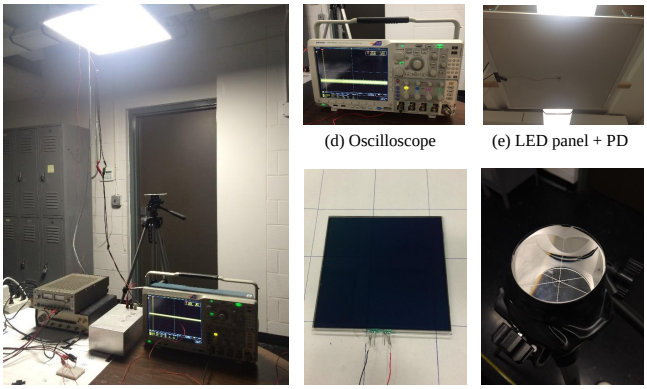

(a) Testbed (b) LCD shutter (c) Retroreflector (d) Oscilloscope (e) LED panel + PD

Fig. 13: Testbed

the PD has not reached to the saturation stage yet. Based on the indication from Fig. 1-10 in [19], we place a light source very close to the PD used in our experiment and observe that the output voltage is very high (several volts) compared to the output voltage (less than 200 milivolts) when only the retroreflected light and the environmental light exist. Therefore, we safely conclude that the PD used in our proposed system is far before reaching to the saturation level and the retroreflected light and the environmental light should be linearly combined. In order to quantify the retroreflected optical power, we subtract the second measurement by the first measurement. We fix the retroreflector on a tripod to perform measurements at different locations and orientations. The testbed is shown in Fig. 13.

5.2 Experiment results

When we perform the measurement of the received optical power without changing the orientation (i.e., zero-value elevation and azimuth angles), we keep the retroreflector at certain height and increase the horizontal distance between the PD and the retroreflector. We observe that the output voltage drops suddenly to zero at a certain horizontal distance when the azimuth angle is non-zero. As shown in Fig. 12, if the azimuth angle is 0°, as the horizontal distance increases, the output voltage decreases smoothly; while if the azimuth angle is 180°, the output voltage suddenly drops to zero when the horizontal distance increases to a certain value. This phenomenon contradicts the isotropic property of circular retroreflectors. After experimentally studying the retroreflector and communicating with the technical support from Thorlabs, we confirm that the reason for the an-isotropic phenomenon is due to the light leaking problem of the three mutually perpendicular reflective surfaces. If the angle of incidence (AOI) to one of the three reflecting surfaces is too

This article has been accepted for publication in a future issue of this journal, but has not been fully edited. Content may change prior to final publication. Citation information: DOI 10.1109/TMC.2019.2901665, IEEE Transactions on Mobile Computing

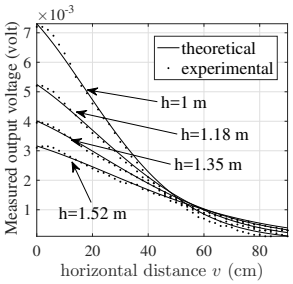

Fig. 14: Theoretical and experimental results of zero-value elevation and azimuth angles setting

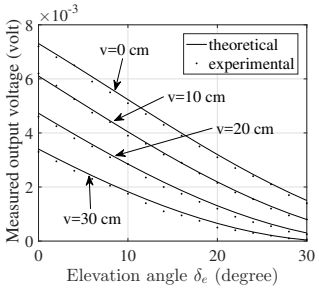

Fig. 15: Theoretical and experimental results of arbitrary-value elevation and azimuth angles setting

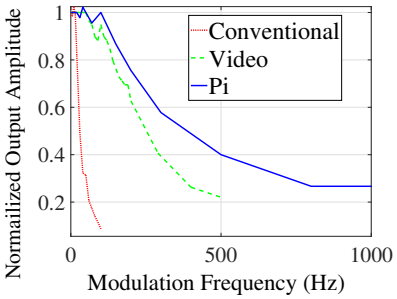

Fig. 16: Signal amplitude vs. modulation frequency for three types of LCD shutters

small, light will be leaking out of the surface instead of being reflected; thus, the total internal reflection (TIO) does not stand anymore. However, the light leaking problem is not a fundamental problem of retroreflectors and can be resolved by re-fabricating three reflecting surfaces to let them reflect as mirrors. Therefore, the isotropic property can hold such that the circular retroreflector is suitable for localization.

To circumvent the light leaking problem, we perform all the experiments at zero azimuth angle, in which case the AOI to each reflecting surface will not be small enough to cause light leaking. To validate the theory in case 1 (equation (7)), we measure the output voltage at 4 different heights; namely, 1 meter, 1.18 meters, 1.35 meters and 1.52 meters. For each height, the measurement is performed at horizontal distances from 0 cm to 90 cm at intervals of 2 cm. The results are shown in Fig. 14. To validate the theory in case 2 (equation (9)), we measure the output voltage at fixed height 1 meter and 4 different horizontal distances; namely, 0 cm, 10 cm, 20 cm and 30 cm. For each horizontal distance, the elevation angle δ_e is varied from 0° to 30° at intervals of 2°. The results are shown in Fig. 15. Since the experimental and the theoretical results match very well, we can safely conclude that the closed-form expression of received optical power when the azimuth angle equals to zero is a very accurate approximation to practical measurements. For the cases where the azimuth angle equals to arbitrary value, the closed-form expression of received optical power is validated by simulations in Sec. 7.1.

6 Experiment Based Evaluation of Localization and Orientation Accuracy

6.1 Applying LCD shutter

In practice, in order to distinguish the reflected light from multiple IoT devices and from environmental reflection, instead of passive opaque chip, an active LCD shutter can be used to cover the front face of retroreflector to modulate the retroreflected light [9], [10]. By transitioning between transparent and opaque states, LCD shutter can approximate a square wave signal at low modulation frequency. To investigate the relationship between signal amplitude and modulation frequency, we measure the signal amplitude by placing three types of LCD shutter (i.e., conventional, video and Pi-cell) between a small LED light bulb and a photodetector (PDA36A from Thorlabs). The results are shown in Fig. 16, it can be seen that the signal amplitude decreases quickly for all three types of LCD shutters. This is due to the long response time (i.e., time cost by transitioning from one state to the other) of LCD shutters. Therefore, we choose a low modulation frequency (20 Hz) to drive the LCD shutter. In the proposed RETRO localization system, the light infrastructure equipped with the PDs is only responsible for generating the DC carrier signal for the retroreflector to send uplink (i.e., from the devices to the PDs mounted on the light infrastructure) optical signals. Therefore, the collision of multiple access only happens at the light source side, which is uplink collision. Different modulation frequencies can be utilized to drive different LCD shutters in order to support multiple access of IoT devices. The capacity of the system and the impact on localization accuracy of mutual interference among different devices will be studied in the future.

In our experiments, Pi-cell is selected as the modulator. It is driven by a function generator. Note that the power consumption of the LCD shutter and its driver circuit is at tens of μW, which is also validated in [9], [10]. Instead of connecting the light intensity measurement circuit to a multimeter, we connect it to an oscilloscope (Tektronix MDO4034-3) and set the sampling rate to 1 MS/s. The recorded data is processed in MATLAB through Fast Fourier Transform (FFT) to compute the signal amplitude. Note that given a certain number of FFT points, the 1st harmonics in frequency domain is linearly proportional to the amplitude of the square wave in time domain. In Fig. 17, we show the FFT plot including retroreflected optical signal (20 Hz) and background light (60 Hz). We can observe that the background noise is much less than the 20 Hz signal amplitude, which enables reliable signal amplitude estimation at the modulation frequency of LCD shutter. The cases where the ambient light (e.g., sunlight) is strong enough to cause the saturation of the PDs rarely happen since the PDs are all attached on the ceiling light source and facing downward.

Besides the modulation frequency, viewing angle also affects the amplitude of the signal produced by LCD shutter. We place the Pi-cell between a small light bulb and a photodetector (PDA36A from Thorlabs) at 8 values of azimuth angles (i.e., 0°, 45°, 90°, 135°, 180°, 225°, 270° and 315°) and 9 values of elevation angles (i.e., 0°, 5°, 10°, 15°, 20°, 25°, 30°, 35° and 40°) to measure the signal amplitude. The results are shown in Fig. 18. When the elevation angle is not larger than 30°, the variation of signal amplitudes for different azimuth angles is very small. However, when the

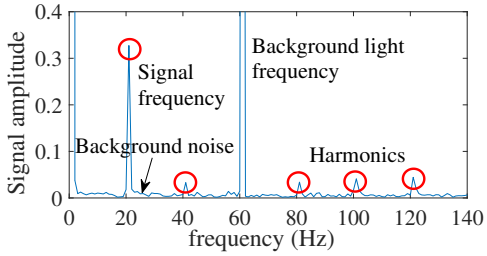

Fig. 17: FFT plot of received signal (low background noise)

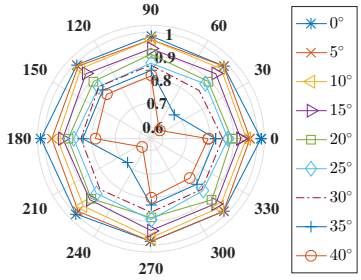

Fig. 18: Normalized signal amplitude vs. different viewing angles

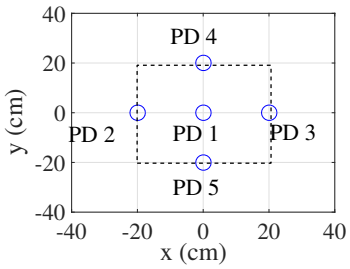

Fig. 19: XY view (top) of PDs in grid structure

elevation angle increases above 30°, the signal amplitudes at azimuth angles of 45° and 225° are much lower than those at other azimuth angles. Therefore, the isotropic property of circular retroreflector may not hold when the incidence angle to the front face of retroreflector is larger than 30°. This issue can be resolved by selecting the closest PDs to perform localization, but it still restricts the orientation range to some extent. Another solution might be using dispersion film instead of LCD shutter, such that the viewing angle issue does not exist. However, the properties and limitations of dispersion film need to be studied thoroughly in the future. In Fig. 18, we can also observe that as the elevation angle of Pi-cell increases from 0° to 30°, the signal amplitude decreases. We use a linear function $\gamma(\theta) = 1 - 0.005\theta$ to approximate the attenuation caused by the viewing angle of Pi-cell, where θ is the incidence angle to the front face of the retroreflector. To compute the received optical power using (9), the right hand side of the equation needs be multiplied by γ^2 since the light rays pass through the Pi-cell twice. Note that by fitting the measurements of received signal strength at different heights to the theoretical values, the value of P_t has taken into account the constant attenuation caused by the transmission rate of the LCD shutter. For different viewing angles, the penetration rate of the LCD shutter will vary and the linear function $\gamma(\theta)$ is approximating the additional attenuation caused by the viewing angle of the LCD shutter.

6.2 Localization and orientation accuracy

Recall that the light leaking problem restricts all the received signal amplitude measurements at zero azimuth angle (Fig. 12). The problem can be handled by manufacturing a corner-cube with three reflecting surfaces as normal mirrors. However, we are using the COTS corner-cube retroreflector, which is designed for laser based applications. Due to the intrinsically isotropic property of circular corner-cube retroreflectors, the light leaking problem caused by laser application-oriented COTS product manufacturing does not hinder the evaluation of localization accuracy. We apply the measurement results using one PD to a realistic localization system, where multiple PDs are mounted on the LED panel in a grid structure with intervals of 20 cm. A central controller is used to monitor the signal amplitudes from all the PDs. Once the central controller detects the signal at certain frequency (20 Hz in our experiment), it selects the PD, whose output signal amplitude is the largest, as the central one and uses the other 4 PDs around the central one to perform the localization algorithm. As shown in Fig. 19, the area within the dashed-line square is the region in which we are evaluating the localization accuracy when the elevation and the azimuth angles of the retroreflector are both zero.

We select 400 positions uniformly within the dashed-line square region and compute the corresponding horizontal distances to each PD. Then we perform the signal amplitude measurement using one PD at all horizontal distances. After we measure the signal amplitudes at 4 different heights (75 cm, 1 m, 1.25 m and 1.5 m), we input them to the RSSI and trilateration based localization algorithm (Sec. 4) to evaluate the localization accuracy. In Fig. 20, we apply our algorithm for 3D localization, in which the height is unknown, and we can observe that, at the height of 1.5 m, the location errors are less than 6 cm in 90% of the cases and the median error is only 2 cm. In Fig 21, the height is known. At the height of 1.5 m, the location errors are less than 2 cm in 90% of the cases and the median error is only 1 cm.

To evaluate both the location and the orientation accuracy, due to the light leaking problem and viewing angle restriction, we only consider PD1, PD2 and PD3 in Fig. 19 to evaluate the elevation angle accuracy when the retroreflector is placed at (0,0) and (10,0) where the height is 1 meter. Note that the viewing angle restriction to valid orientation detection range might be resolved by utilizing dispersion film which needs to be investigated thoroughly, or by leveraging a gyroscope and sending the detected orientation information back to the tracking system via the uplink enabled by the retroreflector. We vary the elevation angle from -10° to 10° when the retrorelector is placed at (0,0) and vary the elevation angle from -5° to 5° when the retroreflector is placed at (10,0). In Fig 22, we apply our 3D localization algorithm, in which the height is unknown, 90% of the location errors are less than 12 cm, 80% of the angular errors are less than 6°, and the median location and angular errors are 3 cm and 2°, respectively. In Fig 23, the height is known, 80% of the location errors are less than 5 cm, 80% of the angular errors are less than 3°, and the median location and angular errors are 1 cm and 1°, respectively. As far as we know, in VLC-based localization systems, Luxapose [3] is the only system that both enables the tracking of devices' orientation and evaluates the orientation accuracy. In our 3D location and orientation results (Fig. 22), using simple and cheap PDs, we are able to achieve parity with the 2D location and orientation results (i.e., height is known) of systems such as Luxapose [3] that requires CMOS imager

This article has been accepted for publication in a future issue of this journal, but has not been fully edited. Content may change prior to final publication. Citation information: DOI 10.1109/TMC.2019.2901665, IEEE Transactions on Mobile Computing

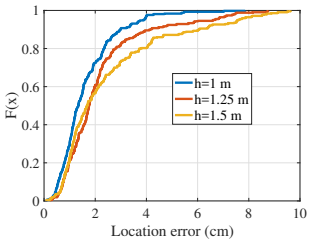

Fig. 20: Empirical CDF of 3D location error

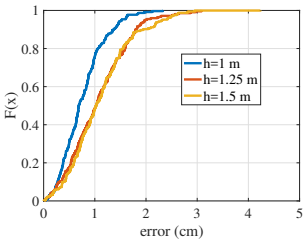

Fig. 21: Empirical CDF of 2D location error

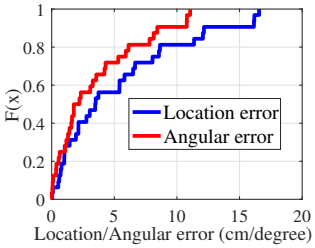

Fig. 22: Empirical CDF of 3D location and orientation error

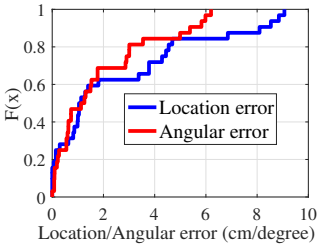

Fig. 23: Empirical CDF of 2D location and orientation error

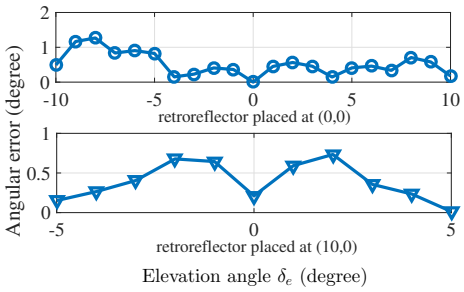

Fig. 24: Orientation error when the location is known

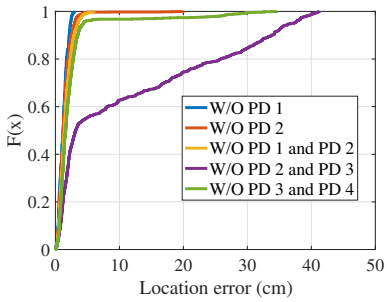

Fig. 25: Empirical CDF of 2D location accuracy when $h = 1.5\ m$ in five different cases: 1) W/O P1; 2) W/O P2; 3) W/O P1 and P2; 4) W/O P2 and P3; 5) W/O P3 and P4.

and heavy computation to obtain angle-of-arrival (AOA) information. In our 2D location and orientation results (Fig. 23), we are able to achieve 40% improvement in both location and orientation accuracy compared to Luxapose.

In Fig. 24, we only evaluate the orientation error from localization. Compared to Luxapose [3], in which the angle error is less than 3° when only orientation is evaluated, we are able to achieve 60% improvement in terms of orientation accuracy. In addition, Luxapose [3] requires four or five customized light beacons to be visible for a camera to achieve decimeter-level location accuracy and roughly 3° orientation error. However, by relying on only one *single slightly modified* light source, RETRO extends the available localization area, within which centimeter-level location accuracy and 1° orientation error can be achieved without requiring computation and heavy sensing, like camera, on the device.

In order to investigate the impact of missing some reflected optical signals on the location accuracy, in Fig. 25, we evaluate the location accuracy when $h = 1.5\ m$ in five different cases: 1) W/O P1; 2) W/O P2; 3) W/O P1 and P2; 4) W/O P2 and P3; 5) W/O P3 and P4. We can observe that removing P1 does not affect the location accuracy at all while removing P2 and P3 renders the localization unreliable. This is because performing localization requires three landmarks that form a triangle on the light source plane. The results indicate that optimizing the deployment of PDs and the strategy of selecting the PDs for localization has the potential of reducing the density of PDs while maintaining the localization performance.

7 Numerical Results

7.1 Simulation based validation of the derivation of received optical power

7.1.1 Objectives of simulation

In Sec. 5, we identify the light leaking problem of circular corner-cube retroreflector PS976 provided by Thorlabs [16]. The light leaking problem, which is elaborated in Fig. 12, limits the azimuth angle δ_a to zero when the total internal reflection property holds. As a consequence, only the cases when $\delta_a = 0°$ are investigated in Sec. 5. In this section, in order to validate the isotropic property (i.e., the retroreflected optical power will not change if the circular retroreflector is only varying its azimuth angle without changing its location and elevation angle) of circular retroreflectors and validate the derivation in Sec. 3-C about the arbitrary value of azimuth angles case, we rely on an open source optical ray tracer BEAM FOUR [20] from Stellar Software to perform ray tracing simulations.

7.1.2 Setup of a ray tracing simulator

BEAM FOUR [20] is a table driven ray tracer. The optical system consisting of surfaces and rays are described by tables of entries. An optical file with extension .OPT is defining the successive optical surfaces to be traced. The sequence of specified surfaces determines the sequence in which the rays are traced. This is a restriction of BEAM FOUR since the tracer presupposes that the sequence of surfaces that the rays arrive at are known. However, the advantage of the sequential ray tracer is computationally efficient. The .OPT table of our proposed RETRO system is shown in Fig. 26. Six surfaces are defined. The first and the fifth rows define the front face of the retroreflector. The type "Iris" is selected for these two surfaces since it does not change the ray direction but defines the maximum radius for ray passage. The first row represents the entrance of retroreflector for the incident rays and the fifth row

RETRO1.OPT row=8 col=71 OPTeditor

6 surfaces RETRO.OPT

X	Y	Z	T	P	R	Types?	F	Dx	Dy	Diam	OffOx	OffOy
0	0	19.1600				Iris				1		
0	0	20	-50.6773	-23.9275	-26.3410	Mirror	S	2.01	2.01		-1	1
0	0	20	50.6773	-23.9275	26.3410	Mirror	S	2.01	2.01		-1	-1
0	0	20		55	45	Mirror	S	2.01	2.01		1	-1
0	0	19.1600				Iris				1		
		0.000001								0.27646		

Front face of retroreflector

Three mutually perpendicular reflective surfaces

Sensing area of photodiode

Fig. 26: The RETRO.OPT table is listing the successive optical surfaces to be traced in the RETRO system.

RETRO.RAY row=6 col=67 RAYeditor

4 rays RETRO.RAY

X0	Y0	U0	V0	W0
-1.14	1.14	-0.5773	0.5773	0.5773
1.14	1.14	0.5773	0.5773	0.5773
-1.14	-1.14	-0.5773	-0.5773	0.5773
1.14	-1.14	0.5773	-0.5773	0.5773

Fig. 27: The RETRO.RAY table is listing a number of rays that are created to probe the optics defined in the optics file with extension .OPT.

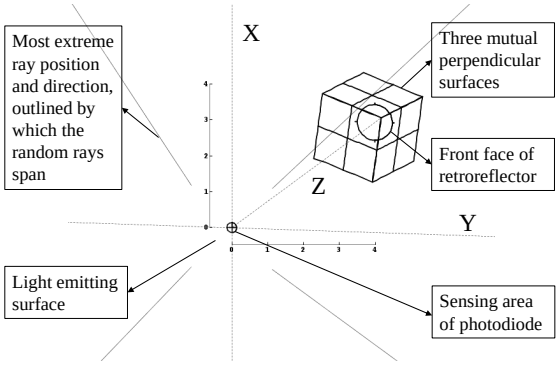

Fig. 28: The system layout is generated by Run::Layout function of BEAM FOUR simulator.

represents the exit of retroreflector for the retroreflected rays. The second, the third and the fourth rows define the three mutually perpendicular reflective surfaces. The type "Mirror" is selected for these three surfaces to enable total internal reflection. The sequence of the three reflective surfaces that an incident ray arrives at is random. Therefore, there are totally six orders of reflection. The example given in Fig. 26 shows one possible order of reflection. The last row defines the sensing area of the PD. The type of the last surface is ignored since the last surface has no action to the arrived rays but only acts as a check point to report the information of the arrived rays. In the second line (i.e., header line) of the RETRO.OPT table, X, Y and Z specify the global coordinates of the vertex of each surface; T, P and R specify the rotated angle of a surface around each axis; F specifies the square/rectangular periphery; Dx and Dy specify the diameters for x and y axes, respectively; Diam specifies the outer periphery of a surface; OffOx and OffOy specify the offset in x and y axes from vertex location, respectively.

In order to evaluate the retroreflected optical power of the optical system defined in RETRO.OPT table, we utilize

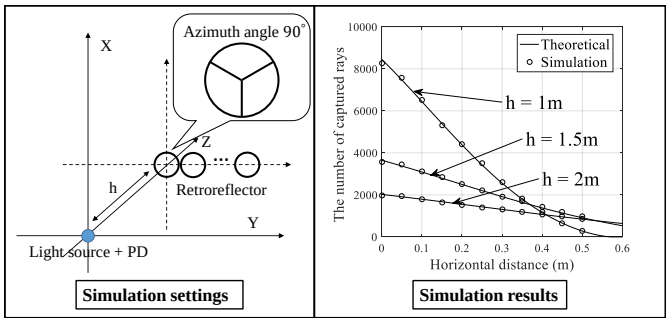

Fig. 29: To validate the isotropic property, the circular corner-cube retroreflector is being moved along the X axis.

the Monte Carlo random ray generator included in BEAM FOUR. The generated random rays span the extent of the overall ray beam outlined by most extreme ray positions and directions defined in the .RAY table. The number of rays that finally reach the last surface (i.e., sensing area of the PD) will be displayed in a pop-up window. Different from calculating the retroreflected optical signal strength through a closed-form equation (analytical results), the ray tracing simulator relies on repeated random sampling to obtain numerical results. The RETRO.RAY table defining the outline rays is shown in Fig. 27. In the second line (i.e., header line) of the RETRO.RAY table, X0 and Y0 specify the starting locations of the outline rays; U0, V0 and W0 specify the directions of the outline rays. It can be seen from the RETRO.RAY table that the light emitting surface is a square area centered at point (0,0,0) with both the width and the length equalling to 2.28 units. In each simulation run with a certain location and a certain orientation of the retroreflector, 500 million random rays are generated based on uniform distribution. Note that the number of retroreflected rays is computed by adding up the outputs of six simulation runs. In each simulation run, the sequence of the three mutually perpendicular reflective surfaces is defined in one of the six orders of reflection. Compared to the experiment settings presented in Sec. 5-A, the value of semi-angle at half power $\psi_{1/2}$ is changed to 60° due to the uniform distribution of random rays, the value of refractive index n is changed to 1 since no substrate material is defined in the RETRO.OPT table, and the value of P_t is estimated by fitting the simulations results at different heights to the theoretical values. The system layout is shown in Fig. 28. The optical system includes a corner-cube retroreflector, a PD and a flat light emitting surface.

This article has been accepted for publication in a future issue of this journal, but has not been fully edited. Content may change prior to final publication. Citation information: DOI 10.1109/TMC.2019.2901665, IEEE Transactions on Mobile Computing

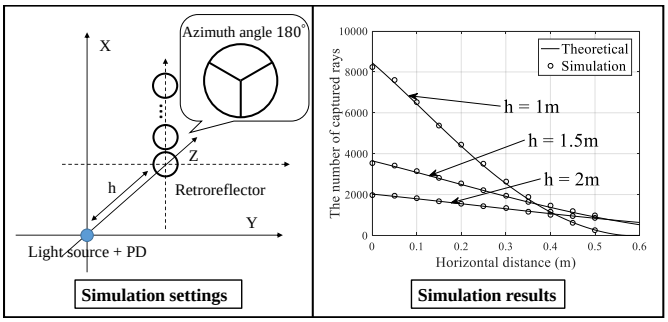

Fig. 30: To validate the isotropic property, the circular corner-cube retroreflector is being moved along the Y axis.

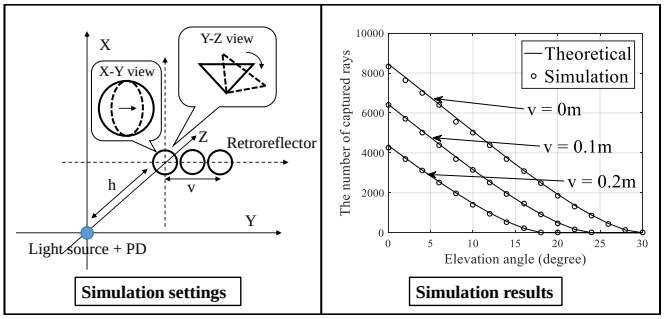

Fig. 31: To validate the theoretical results when azimuth angle is arbitrary. Elevation angle is varied at different locations when azimuth angle is zero.

7.1.3 *Validation of the derivation of received optical power*

To validate the isotropic property of circular retroreflectors, which is not validated in Sec. 5 due to the light leaking problem, we perform two sets of simulations that are similar to the experiments of which the results are shown in Fig. 14. In the first set of simulations, the azimuth angle is set to 90° and the retroreflector is being moved along the X axis at three different heights; namely, 1 meter, 1.5 meters and 2 meters. For each height, the simulation is performed at horizontal distances from 0 cm to 50 cm at intervals of 5 cm. The simulation settings and the simulation results are shown in Fig. 29. The simulation settings of the second set of simulations are similar to that of the first set except that the azimuth angle is set to 180° and the retroreflector is being moved along the Y axis. The simulation settings and results of the second set are shown in Fig. 30. We can observe that the simulation results of both sets and the theoretical results match very well. Therefore, if the circular retroreflector is only altering its azimuth angle without changing its location and elevation angle, the amount of retroreflected rays will not change (i.e., isotropic property).

To validate the theoretical derivation in Sec. 3-C about the arbitrary value of azimuth angles case, we perform simulations that are similar to the experiments of which the results are shown in Fig. 15. The azimuth angle is set to 0° and the retroreflector is placed at fixed height 1 meter and three different horizontal distances; namely, 0 cm, 10 cm and 20 cm. For each horizontal distance, the elevation angle is varied from 0° to 30° at intervals of 2°. The simulation settings and results are shown in Fig. 31. After that, we perform another set of simulations where the retroreflector is placed at (10 cm, 10 cm, h) and its azimuth angle is set

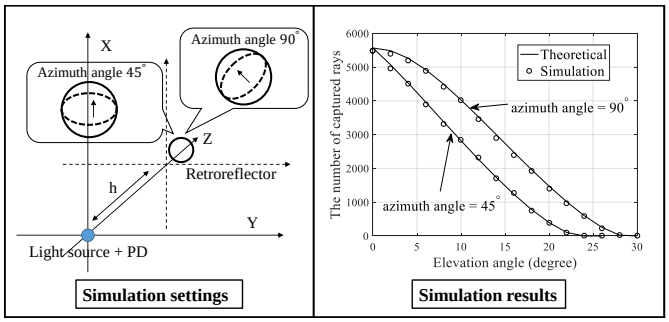

Fig. 32: To validate the theoretical results when azimuth angle is arbitrary. Elevation angle is varied when azimuth angle is NOT zero.

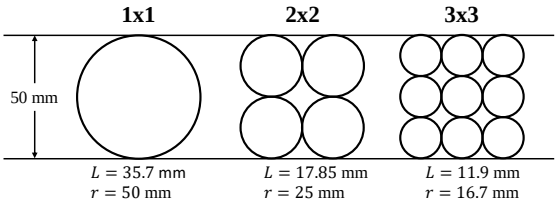

Fig. 33: Fixing the length and the width of a retroreflector array, three cases (i.e., 1x1, 2x2 and 3x3) are investigated. As the diameter of each circular retroreflector decreases, the thickness L of the retroreflector array is reduced.

to 45° and 90°, respectively. For each case of azimuth angle, the elevation angle is varied from 0° to 30° at intervals of 2°. The simulation settings and results are shown in Fig. 32. We can observe that the simulation results and the theoretical results in both Fig. 31 and Fig. 32 match very well. Therefore, similar to the conclusion drawn from experiments, we safely conclude that the closed-form expression of received optical power when the azimuth angle equals to arbitrary value is a very accurate approximation to practical measurements.

7.2 Thickness of retroreflector

One issue of the circular corner-cube retroreflector used in the experiments is the thickness. According to the structure of a circular corner-cube retroreflector, given the diameter r of the front face, the minimum thickness is $\frac{r}{2\tan 35^\circ}$. In order to achieve the localization performance presented in

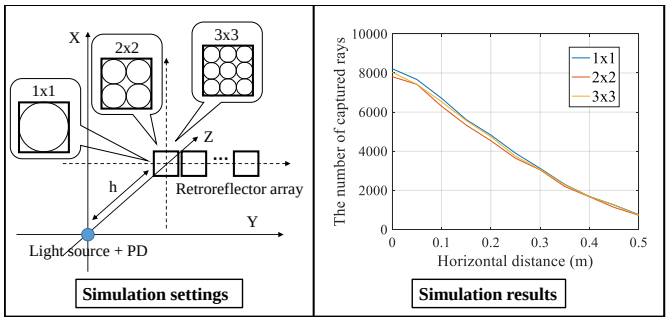

Fig. 34: To evaluate the retroreflected optical signal strength of different retroreflector arrays, three types (i.e., 1x1, 2x2 and 3x3) of retroreflector array are being moved along the X axis.

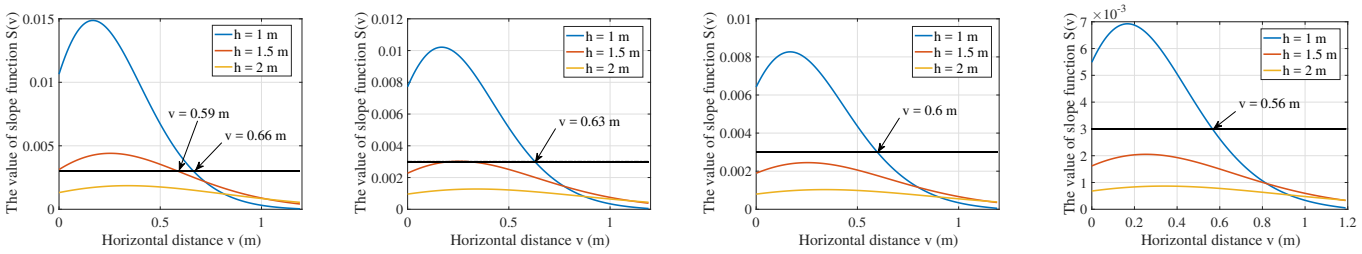

(a) $\psi_{1/2} = 33°$ (b) $\psi_{1/2} = 40°$ (c) $\psi_{1/2} = 45°$ (d) $\psi_{1/2} = 50°$

Fig. 35: The value of slope function $S(v)$ vs. the horizontal distance v when the semi-angle at half power $\psi_{1/2}$ is increasing: (a) $\psi_{1/2} = 33°$; (b) $\psi_{1/2} = 40°$; (c) $\psi_{1/2} = 45°$; (d) $\psi_{1/2} = 50°$.

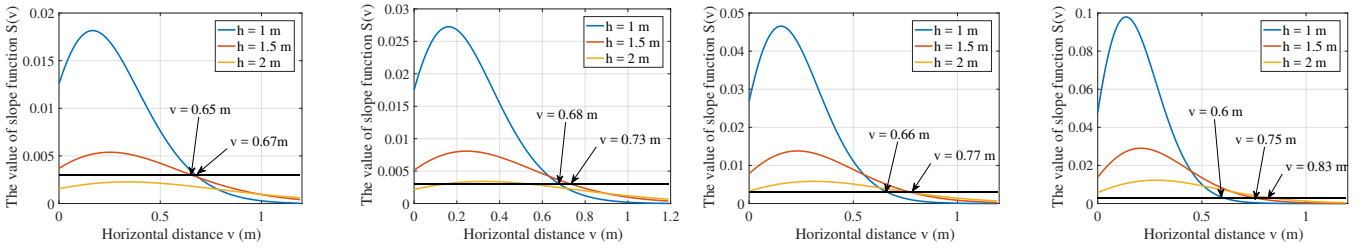

(a) $\psi_{1/2} = 30°$ (b) $\psi_{1/2} = 25°$ (c) $\psi_{1/2} = 20°$ (d) $\psi_{1/2} = 15°$

Fig. 36: The value of slope function $S(v)$ vs. the horizontal distance v when the semi-angle at half power $\psi_{1/2}$ is decreasing: (a) $\psi_{1/2} = 30°$; (b) $\psi_{1/2} = 25°$; (c) $\psi_{1/2} = 20°$; (d) $\psi_{1/2} = 15°$.

Sec. 6, the minimum thickness is 35.7 mm, which does not include the unnecessary recessed length. To reduce the thickness, one possible solution is to adopt retroreflector array. Retroreflector array combines multiple circular retroreflectors with smaller diameter of the front faces such that the thickness of the retroreflector array is less than that of a single retroreflector. Applications of retroreflector array include road signs and bicycle retroreflectors. As shown in Fig. 33, fixing the length and the width, three cases (i.e., 1x1, 2x2 and 3x3) of retroreflector array are plotted. Compared to the single retroreflector case (i.e., 1x1), 2x2 and 3x3 retroreflector arrays reduce the thickness by 50% and 66%, respectively. To evaluate the levels of the retroreflected optical signal strength for the three cases of retroreflector array, we perform simulations similar to that in Fig. 29. For each case of retroreflector array, the simulation is performed at horizontal distances from 0 cm to 50 cm at intervals of 5 cm. The simulation settings and results are shown in Fig. 34. The retroreflected optical power stays at the same level for 1x1, 2x2 and 3x3 retroreflector arrays. For 2x2 retroreflector array, the diameter of the front face of each circular retroreflector is reduced by half, thus the retroreflected optical power is expected to be reduced to approximately $1/4$ since the effective reflecting area (Fig. 7) is reduced to approximately $1/4$. Therefore, the total retroreflected optical power of the four circular retroreflectors on the 2x2 retroreflector array is similar to that of the 1x1 case. The results indicate that retroreflector array is a viable solution to reduce the thickness while keeping the localization performance at the same level.

7.3 Range of the localization system.

For RF-based localization systems, due to the omnidirectional signal propagation, the range of the localization system is generally evaluated in one dimension. However, for VLC-based localization systems, due to the directional signal propagation of light sources, the range we discuss here is in two dimensions, which are the height h and the horizontal distance v (refer to Fig. 2a). As a preliminary investigation, we only consider the cases when the elevation angle $\delta_e = 0°$. Recall that in Fig. 14, the retroreflected optical power is shown for four different heights and for each height the horizontal distance spans from 0 cm to 90 cm. We can observe that as the height increases, the absolute value of the slope of the corresponding curve decreases. In other words, as the height increases, the difference of retroreflected optical power between two adjacent positions is getting smaller, which indicates worse distinguishability among different locations due to RSSI-based localization approach. Therefore, we utilize a slope function $S(v)$ to estimate the localization performance at a specific range. Based on the same settings presented in Sec. 5-A, we compute the retroreflected optical power vs. the horizontal distance for three different heights; namely 1 meter, 1.5 meters and 2 meters. After that, we compute the value of the slope function $S(v)$ for the generated three curves. The results are shown in Fig. 35a. According to the localization performance presented in Sec. 6, we add a heuristic threshold, which is the black line in Fig. 35a. If the slope value is above the threshold, we consider the localization performance to be acceptable and vice versa. Based on the heuristic threshold and the results shown in Fig. 35a, we conclude that the maximum horizontal distance $v = 0.59\ m$ when the height $h = 1.5\ m$ and any location on the horizontal plane when the height $h = 2\ m$ is out of the range of the localization system. The localization performance presented in Sec. 6 can be achieved everywhere when light infrastructure is densely deployed. For a typical retail settings with ceiling lamps, the

localization performance can be achieved every few meters, perhaps with dead reckoning filling in the gaps. An intuitive answer for how to enlarge the range of the localization system might be having a wider-angle light source. To investigate the impact of altering the value of semi-angle at half power $\psi_{1/2}$ on the range of the localization system, we compute $S(v)$ when $\psi_{1/2} = 40°, 45°$ and $50°$, and the results are shown in Fig. 35b, Fig. 35c and Fig. 35d, respectively. It can be observed that, as $\psi_{1/2}$ increases, the range of the localization system reduces. This is because as $\psi_{1/2}$ is getting larger, given a specific height, the distribution of optical power on the horizontal plane is becoming more uniform, which indicates worse distinguishability among different locations. Will reducing $\psi_{1/2}$ improve the range? To answer this question, we compute $S(v)$ when $\psi_{1/2} = 30°, 25°, 20°$ and $15°$, and the results are shown in Fig. 36. It can be observed that as $\psi_{1/2}$ increases, the vertical range (i.e., the height h) increases. However, the horizontal ranges when $h = 1\ m$ for different $\psi_{1/2}$'s are 0.67 m, 0.68 m, 0.66 m and 0.6 m, respectively. The horizontal ranges when $h = 1.5\ m$ for different $\psi_{1/2}$'s are 0.65 m, 0.73 m, 0.77 m and 0.75 m, respectively. Therefore, based on the settings presented in Sec. 5-A, the best $\psi_{1/2}$'s for localizing a device on the horizontal plane when $h = 1\ m$ and when $h = 1.5\ m$ are between $25°$ and $20°$ and between $20°$ and $15°$, respectively. Depending on the specific value of h, there exists an optimal $\psi_{1/2}$ that maximizes the horizontal range.

8 Discussion

Size and deployment of PDs. In our proposed RETRO system, densely deployed PDs on the light emitting surface can improve the localization performance by taking advantage of more reliable landmarks. However, the dense deployment of PDs might introduce a critical problem to illumination since they are blocking the line-of-sight (LOS) path. The size of the PDs needs to be much less than that of the front face of a single retroreflector. However, smaller size of PDs will lead to weaker received signal strength, which may lower the localization performance. Referring to COTS Silicon PIN photodidoe T330P [21], the size of a single PD can be reduced to less than 0.5 mm^2. The wiring process of such small PD needs advanced manufacturing procedures. Therefore, we will study in the future the system performance evaluation of such small-size PD and the optimal size and deployment of PDs to maximize the coverage and localization performance while producing minimal impact on indoor illumination and taking in account scalability, robustness and accuracy.

Different light sources and light emission patterns. In our proof-of-concept setup, we utilize a flat LED panel with light evenly distributed on the light emitting surface. If the light source is irregular (i.e., the light emitting surface plane is not flat or the light is not evenly distributed across the light emitting surface), the received optical power will not be linearly proportional to the area of light source from which the light rays are retroreflected back to the PD. Also Lambertian emission model might not be suitable for modeling emission pattern of every small spot of light emitting surface. The accuracy of modeling light distribution and light emission pattern will directly affect the accuracy of the RSSI and trilateration based localization. To accurately model these two factors, different types of lamps that are generally used for indoor illumination need to be studied. The modeling process needs the effective reflecting area around the PD to be isotropic. Once the requirement is satisfied, the modeling process can be done by limiting the light emitting surface to a small region (maximum effective reflecting area) and measuring the light distribution on the horizontal localization plane. The measured light distribution will determine the proper value of semi-angle at half power or even another distribution model other than Lambertian distribution.

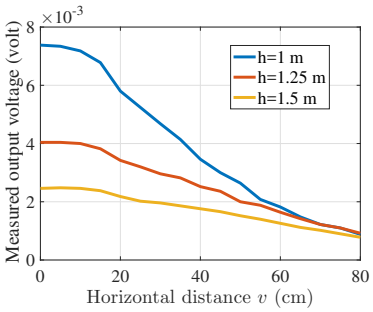

Fig. 37: Experimental results for retroreflective sheet (9 cm x 9 cm) based on the same experimental setup of Sec. 5

Different types of retroreflector. In addition to a single circular structural corner-cube retroreflector or retroreflector array, the retroreflection model of retroreflective sheet and retroreflective spray paint needs to be investigated. Modeling of retroreflective sheeting has been studied in transportation applications [22], such as traffic sign. However, applying the retroreflective sheeting material and also spray paint to our proposed localization system is still unexplored. It is worth studying the basic three types of materials (i.e, enclosed glass beads or lens, encapsulated glass beads, and prismatic) used in the construction of traffic signs, and integrate them into our localization model. To evaluate the distinguishability of the low-cost retroreflective sheet, we perform the same experiments as those described in Sec. 5 for a 9 cm x 9 cm retroreflective sheet manufactured by 3M Scotchlite. The results are shown in Fig. 37. Based on the distinguishability indicated by the experimental results, the low-cost retroreflective sheet with the size of the front face larger than that of the corner-cube retroreflector can achieve comparable localization performance.

Localization algorithm. In order to obtain the five unknowns (i.e., $x_0, y_0, z_0, \delta_a, \delta_e$) that represent the location and orientation of the retroreflector, generally a non-linear least square optimization problem needs to be resolved. In our proof-of-concept system setup, the widely-used Levenberg-Marquardt algorithm [4] is adopted. For fast-moving object, the localization algorithm needs to be completed in an extremely short period. Therefore, it is worth studying the trade-off between the cost of algorithm and the achieved localization accuracy to dynamically adjust the localization algorithm to accommodate objects with different moving speeds.

Shutter speed and system capacity. The trade off between the shutter speed (modulation frequency) and the

System	Epsilon	Luxapose	PIXEL	Litell	Navilight	RETRO
Reference	[2]	[3]	[4]	[5]	[6]	[this]
Location accuracy (90%)	0.4 m	0.1 m	0.3 m	0.1 m	1 m	2 cm
Orientation accuracy	N/A	3°	N/E	N/A	N/A	1°
Method	Model	AoA	AoA	FP	FP	Model
Database	No	Yes	Yes	Yes	Yes	No
Unmodified infrastructure	No	No	Yes	Yes	Yes	Yes
Require multiple light sources	Yes	Yes	No	No	No	No
Require camera	No	Yes	Yes	Yes	Yes	No

TABLE 1: Comparison with VLC-based localization systems. N/E stands for not evaluated. FP and AoA are fingerprinting and angle-of-arrival, respectively.

capacity of the system (i.e., the number of devices tracked simultaneously) is an important problem. The higher the maximum shutter speed is, more devices can be supported simultaneously. Since the output signal amplitude decreases as the modulation frequency (shutter speed) increases, the device that is utilizing the higher modulation frequency would be better to have larger reflecting area in order to ensure the reliability of the retroreflected optical signal. The interference among different channels and their harmonics also needs to be considered when separating the channels.

9 Related work

RF-based localization approaches. RFID [23] is already a solution to indoor localization when the very early IoT applications have been developed. Passive RFID technology works only in the proximity of specialized RFID readers, providing a 'point-in-time' location. Active RFID tags extend the localization range by self-broadcasting identity information periodically. Although RFID tags are cheap, the localization accuracy (less than 1 meter) depends on densely deployed RFID readers, which are very expensive. When applying RFID to health care, electromagnetic interference (EMI) from RFID to medical equipment is also a critical problem, for example, 34 incidents out of 123 EMI tests are reported in [24]. Utilizing existing infrastructure, WiFi-based localization [25], [26] can localize and monitor WiFi-enabled devices within large range (e.g. 150 meters). However, it is difficult for WiFi-based localization approach to achieve the level of accuracy afforded by RFID and BLE. Although in the most recent WiFi-based localization works [25], [26], authors claim that WiFi-based localization approach can achieve decimeter-level accuracy, the location error reaches to several meters at the 80th percentile, which can cause destructive outcome for some location error sensitive applications. In addition, executing localization process will affect user devices' TCP throughput [26]. BLE is already applied to commercial products, such as ibeacon [27]. BLE-based localization achieves better accuracy than WiFi-based localization and it embraces advantages like cost-efficiency and flexibility. However, BLE-based localization is intrinsically low frequency radio (i.e. use the same spectrum as WiFi). Therefore, the location error can still reach to meter-level and the interference to WiFi-based user devices is considerable. UWB-based localization [28] is able to achieve location precision within tens of centimeters due to the fact that the signals maintain their integrity and structure even in the presence of noise and multi-path effects. Nevertheless, the high cost of hardware, shorter battery lifetime than BLE, and lack of interaction with the current devices render UWB-based localization not being used universally. Signals do not penetrate walls, such as infrared or ultrasound, tend to provide more accurate localization in an indoor environment because only devices that have line of sight (LOS) can communicate. However, beam alignment and additional hardware cost limit their applicable scenarios.

VLC-based localization approaches. Existing VLC based localization works are not suitable for real-time tracking of passive IoT devices not only because of the absence of backward channel. Epsilon [2] and Luxapose [3] require modified light infrastructure by adding extra driver circuit. Litell [5] requires specific unmodified light source like fluorescent lamp. Luxapose [3] and PIXEL [4] require a power-consuming camera facing upward to keep capturing images containing enough landmarks. Navilight [6] requires the object to move for a certain distance to collect light intensity pattern. Based on existing light infrastructure with any slightly modified light source, RETRO is capable of determining the position and the orientation of any passive IoT devices with ultra-low power and no camera, expensive sensor, or computational capability at the devices. Although [4], [5], [6] are able to execute localization based on a single light source, they either necessitate camera to enable image processing [4], [5], or cannot localize static objects [6]. Utilizing a single light source, RETRO can achieve centimeter-level location accuracy and single-digit orientation error. A comparison with VLC-based localization systems is summarized in Table 1.

10 Conclusion

In this paper, we propose and prototype RETRO, which to the best of our knowledge for the first time enables backward channel from the object to landmarks for VLC-based localization systems. Embracing all the advantages of VLC-based localization approach, such as high accuracy, orientation sensitivity, no interference to RF-based devices, RETRO is capable of utilizing any single slightly modified light source to execute real-time tracking of location and orientation of any passive IoT device with ultra-low power and no computational capability at the devices. Theoretically derived closed-form expression of received optical power is validated by experiments and ray tracing based simulation. A set of extensive experimental results demonstrate that RETRO achieves remarkably good performance, and centimeter-level location error (i.e., less than 2 cm location error at 90% of the time) as well as up to 1° orientation error. The thickness of the retroreflector and the range of the

localization system are further investigated for practicality concerns.

ACKNOWLEDGMENTS

This work was supported in parts by NSF grants CNS-1617924 and EEC-1560131.

REFERENCES

[1] P. Bahl and V. N. Padmanabhan, "RADAR: An in-building RF-based user location and tracking system," in *IEEE INFOCOM*, vol. 2, 2000, pp. 775–784.
[2] L. Li, P. Hu, C. Peng, G. Shen, and F. Zhao, "Epsilon: A Visible Light Based Positioning System," in *USENIX NSDI*, 2014, pp. 331–343.
[3] Y.-S. Kuo, P. Pannuto, K.-J. Hsiao, and P. Dutta, "Luxapose: Indoor positioning with mobile phones and visible light," in *ACM MobiCom*, 2014, pp. 447–458.
[4] Z. Yang, Z. Wang, J. Zhang, C. Huang, and Q. Zhang, "Wearables can afford: Light-weight indoor positioning with visible light," in *ACM MobiSys*, 2015, pp. 317–330.
[5] C. Zhang and X. Zhang, "LiTell: Robust indoor localization using unmodified light fixtures," in *ACM MobiCom*, 2016, pp. 230–242.
[6] Z. Zhao, J. Wang, X. Zhao, C. Peng, Q. Guo, and B. Wu, "NaviLight: Indoor Localization and Navigation Under Arbitrary Lights," in *IEEE INFOCOM*, 2017.
[7] T. Li, C. An, Z. Tian, A. T. Campbell, and X. Zhou, "Human sensing using visible light communication," in *ACM MobiCom*, 2015.
[8] T. Starner, B. Leibe, D. Minnen, T. Westyn, A. Hurst, and J. Weeks, "The perceptive workbench: Computer-vision-based gesture tracking, object tracking, and 3d reconstruction for augmented desks," *Machine Vision and Applications*, vol. 14, no. 1, pp. 59–71, 2003.
[9] J. Li, A. Liu, G. Shen, L. Li, C. Sun, and F. Zhao, "Retro-VLC: Enabling battery-free duplex visible light communication for mobile and iot applications," in *ACM HotMobile*, 2015, pp. 21–26.
[10] S. Shao, A. Khreishah, and H. Elgala, "Pixelated VLC-backscattering for self-charging indoor IoT devices," *IEEE Photonics Technology Letters*, vol. 29, no. 2, pp. 177–180, 2017.
[11] X. Xu, Y. Shen, J. Yang, C. Xu, G. Shen, G. Chen, and Y. Ni, "PassiveVLC: Enabling practical visible light backscatter communication for battery-free iot applications," in *ACM MobiCom*, 2017, pp. 180–192.
[12] A. Lundvall, F. Nikolajeff, and T. Lindström, "High performing micromachined retroreflector," *Optics express*, 2003.
[13] Reflect-All, https://reflect-all.com/, [Online; accessed 2-May-2017].
[14] D. A. Arnold, "Method of calculating retroreflector-array transfer functions," *SAO Special Report*, vol. 382, 1979.
[15] T. Komine and M. Nakagawa, "Fundamental analysis for visible-light communication system using LED lights," *IEEE Transactions on Consumer Electronics*, vol. 50, no. 1, pp. 100–107, 2004.
[16] Thorlabs, https://www.thorlabs.com/newgrouppage9.cfm?objectgroup_id=145, [Online; accessed 1-April-2017].
[17] Refractive index database, https://refractiveindex.info/?shelf=glass&book=BK7&page=SCHOTT, [Online; accessed 2-May-2017].
[18] Hamamatsu, https://www.hamamatsu.com/resources/pdf/ssd/s6801_etc_kpin1046e.pdf, [Online; accessed 1-April-2017].
[19] ——, https://www.hamamatsu.com/resources/pdf/ssd/e02_handbook_si_photodiode.pdf, [Online; accessed 1-April-2017].
[20] Stellar Software, https://www.stellarsoftware.com/, [Online; accessed 1-September-2017].
[21] Vishay, https://www.vishay.com/docs/83490/t330p.pdf, [Online; accessed 1-April-2017].
[22] G. W. Flintsch, "Review of retroreflective sign sheeting materials, practices and policies. final report," Tech. Rep., 1993.
[23] B. Alsinglawi, M. Elkhodr, Q. V. Nguyen, U. Gunawardana, A. Maeder, and S. Simoff, "RFID Localisation for Internet of Things Smart Homes: A Survey," *IJCNC*, vol. 9, no. 1, 2017.
[24] R. Van Der Togt, E. J. van Lieshout, R. Hensbroek, E. Beinat, J. M. Binnekade, and P. Bakker, "Electromagnetic interference from radio frequency identification inducing potentially hazardous incidents in critical care medical equipment," *Jama*, vol. 299, no. 24, pp. 2884–2890, 2008.
[25] M. Kotaru, K. Joshi, D. Bharadia, and S. Katti, "Spotfi: Decimeter level localization using wifi," in *ACM SIGCOMM*, 2015.
[26] D. Vasisht, S. Kumar, and D. Katabi, "Decimeter-Level Localization with a Single WiFi Access Point," in *USENIX NSDI*, 2016.
[27] Apple Inc., https://developer.apple.com/ibeacon/, [Online; accessed 4-May-2017].
[28] Decawave, https://www.decawave.com/, [Online; accessed 4-May-2017].

Sihua Shao received the B.S. degree in electrical and information engineering from South China University of Technology in 2011, the M.S. degree in electrical and information engineering fro Hong Kong Polytechnic University in 2012, and the Ph.D. degree in electrical and computer engineering from New Jersey Institute of Technology. He is currently a Post Doctoral Research Associate with the Department of Electrical and Computer Engineering, New Jersey Institute of Technology. His current research interests include wireless communication, Internet-of-Things, visible light communication and positioning, heterogeneous network, cyber-physical system and ultra-low power system.

Abdallah Khreishah received his Ph.D and M.S. degrees in Electrical and Computer Engineering from Purdue University in 2010 and 2006, respectively. Prior to that, he received his B.S. degree with honors from Jordan University of Science & Technology in 2004. During the last year of his Ph.D, he worked with NEESCOM. In Fall 2012, he joined the ECE department of NJIT where he is currently an Associate Professor. Abdallah is an active researcher. His research spans the areas of visible-light communications, network coding, wireless networks, congestion control, cloud computing, network security, intellegent transportation sysytems, and database systems for large projects. His research projects are funded by the National Science Foundation (NSF), New Jersey Department of Transportation (NJDOT), and the UAE Research Foundation.

Issa Khalil received PhD degree in Computer Engineering from Purdue University, USA in 2007. Immediately thereafter he joined the College of Information Technology (CIT) of the United Arab Emirates University (UAEU) where he served as an associate professor and department head of the Information Security Department. In 2013, Khalil joined the Cyber Security Group in the Qatar Computing Research Institute (QCRI), a member of Qatar Foundation, as a Senior Scientist, and a Principal Scientist since 2016. Khalils research interests span the areas of wireless and wireline network security and privacy. He is especially interested in security data analytics, network security, and private data sharing. His novel technique to discover malicious domains following the guilt-by-association social principle attracts the attention of local media and stakeholders, and received the best paper award in CODASPY 2018. Dr. Khalil served as organizer, technical program committee member and reviewer for many international conferences and journals. He is a senior member of IEEE and member of ACM and delivers invited talks and keynotes in many local and international forums. In June 2011, Khalil was granted the CIT outstanding professor award for outstanding performance in research, teaching, and service.